Mon. Not. R. Astron. Soc. **000**, 1–16 (2012) Printed 6 September 2012 (MN LATEX style file v2.2)

A New Model for the Milky Way Bar

Yougang Wang[1,2⋆], Hongsheng Zhao[2,3,4], Shude Mao[2,5], R. M. Rich[6]
[1] *Key Laboratory of Optical Astronomy, National Astronomical Observatories, Chinese Academy of Sciences, Beijing 100012, China*
[2] *National Astronomical Observatories, Chinese Academy of Sciences, Beijing 100012, China*
[3] *SUPA, University of St Andrews, KY16 9SS, UK*
[4] *Vrije Universiteit, De Boelelaan 1081, 1081 HV Amsterdam, The Netherlands*
[5] *Jodrell Bank Centre for Astrophysics, University of Manchester, Manchester M13 9PL, UK*
[6] *Department of Physics and Astronomy, University of California, Los Angeles, CA 90095-1562, USA*

Accepted . Received .

ABSTRACT
We use Schwarzschild's orbit-superposition technique to construct self-consistent models of the Galactic bar. Using χ^2 minimisation, we find that the best-fit Galactic bar model has a pattern speed $\Omega_{\rm p} = 60$ km s^{-1} kpc^{-1}, disk mass $\rm M_d = 1.0 \times 10^{11} M_\odot$ and bar angle $\theta_{\rm bar} = 20^\circ$ for an adopted bar mass $\rm M_{bar} = 2 \times 10^{10} M_\odot$. The model can reproduce not only the three-dimensional and projected density distributions but also velocity and velocity dispersion data from the BRAVA survey. We also predict the proper motions in the range $l = [-12^\circ, 12^\circ]$, $b = [-10^\circ, 10^\circ]$, which appear to be higher than observations in the longitudinal direction. The model is stable within a timescale of 0.5 Gyr, but appears to deviate from steady-state on longer timescales. Our model can be further tested by future observations such as those from GAIA.

Key words: Galaxy: bulge - Galaxy: centre - Galaxy: structure - Galaxy: general - Galaxy: nucleus - Galaxy: formation

1 INTRODUCTION

It is well known that most spiral galaxies host a bar structure in their central region (e.g. Lee et al. 2011). Therefore, one of the most important issues in galaxy formation and evolution is to understand the structure and dynamical properties of barred galaxies. Our own Milky Way is the nearest barred galaxy. Compared with other distant galaxies, the Galaxy has extensive observed photometric and kinematic data which enable us to study the bar structure in detail. A thorough understanding of the structure and dynamics of the Galactic bar may help us understand the formation of other spiral galaxies, and test the validity of the popular Cold Dark Matter structure formation model (e.g. Shen et al. 2010).

Observationally, the Galactic bar model can be constrained by surface brightness maps (Dwek et al. 1995; Babusiaux & Gilmore 2005; Gonzalez et al. 2011), microlensing optical depth maps (Blitz & Spergel 1991; Zhao et al. 1995) and star counts (Stanek et al. 1994; Mao & Paczyński 2002; Rattenbury et al. 2007). Different observational techniques, wavelengths and fields probe different aspects of the bar. Schwarzschild's orbit-superposition technique (Schwarzschild 1979) provides us the possibility to construct a model that can fit all observations. Using the orbit-superposition technique, Zhao (1996, hereafter ZH96) constructed a self-consistent Galactic bar model, which can fit the surface brightness, velocity and velocity dispersion in the Baade's window (BW). However, recently it was found that the predicted rotation curve in ZH96 is inconsistent with the results from the Bulge Radial Velocity Assay (BRAVA, Rich et al. 2007; Howard et al. 2008; Kunder et al. 2012). Possible explanations are (1) the data resolution in ZH96 is not sufficiently high, and/or (2) the initial conditions of orbits include too many loop orbits. Also using the orbit-superposition technique, Häfner et al. (2000) constructed a dynamical model of the inner Galaxy, which fits most of the available data in one very intensively observed bulge field, Baade's Window $(l, b) = (0, -4)$; the only disadvantage is that the proper motion dispersion in their model is higher than the measured values by Spaenhauer et al. (1992). Another useful method to generate self-consistent dynamical models is the made-to-measure algorithm (Syer & Tremaine 1996; de Lorenzi et al. 2007; Dehnen 2009; Long & Mao 2010), which was implemented for the Milk Way by Bissantz et al. (2004). However, only the density map of Milk Way was used to construct the dynamical model, no kinematic constraints were applied and their effective field is small. Furthermore, the effective particle number in their study turns out to be small (only a few thousand, Rattenbury et al. 2007).

Recently, extensive observations of the central re-

⋆ email: wangyg@bao.ac.cn

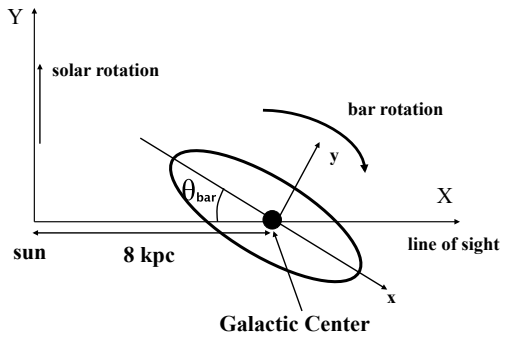

Figure 1. The coordinate system used throughout the paper. The major axis (x-axis) of the bar is misaligned with the line of sight (X-axis) with an angle $\theta_{\rm bar}$. The z-axis comes out of the page. The bar rotation and the rotation of the Sun with respect to the Milky Way centre are indicated. Notice the rotation of the bar is in the negative z-axis and the near-side of the bar has positive longitude (l).

gion of the Milky Way by the Hubble Space Telescope (Kozłowski et al. 2006) and ground-based telescopes (BRAVA: Rich et al. 2007; Howard et al. 2008; Kunder et al. 2012; OGLE: Udalski et al. 2000; Sumi et al. 2004) provide many other large samples of kinematic data. In this paper, our aim is to construct a self-consistent and stable bar model which can fit all the presently-available observed data in the central region of the Milky Way by using the Schwarzschild method. As we will see later, we are able to produce a self-consistent model, but there are issues with long term stability.

The paper is organized as follows. In section 2, we describe the density and potential model for this study. Section 3 presents the details of our implementation of the Schwarzschild method. In section 4, we show the main results. Section 5 shows the stability of the bar model. Conclusion and discussion are given in section 6. Throughout this paper, we adopt the distance to the Galactic center as $R_0 = 8$ kpc.

2 DENSITY AND POTENTIAL OF THE CENTRAL REGION OF THE GALAXY

For clarity, in Figure 1, we first establish the coordinate system we use throughout this paper. In particular, the major axis of the bar is along the x-axis, and is at an angle $\theta_{\rm bar}$ with respective to the line of sight (the X-axis). Notice that the bar angular momentum is along the negative z-axis, but we still write the pattern speed as positive for abbreviation.

2.1 Density and potential of the bar and bulge

Lots of observation data have been used to constrain dynamical models of the Galaxy. Using the *COBE* DIRBE multiwavelength observations, Dwek et al. (1995) constructed many analytic bar models. Stanek et al. (1997), Babusiaux & Gilmore (2005) and Rattenbury et al. (2007) used the star counts of the red clump giant stars to constrain the triaxial Galactic bar models. Both Stanek et al. (1997) and Rattenbury et al. (2007) found the analytic bar model given in Dwek et al. (1995) fit the data well. In this paper, we also adopt the Dwek et al. (1995) bar model as in ZH96, which has the following form

$$\rho(x,y,z) = \rho_0 \left[\exp\left(-\frac{r_1^2}{2} \right) + r_2^{-1.85} \exp(-r_2) \right], \quad (1)$$

where the first term represents a bar with a Gaussian radial profile and the second term a spheroidal nucleus with a steep inner power law and an exponential outer profile. In this paper, we refer both the bar and nuclear components simply as the "bar". The central density ρ_0 is determined by normalising the total mass of the bar, $M_{\rm bar} = 2.0 \times 10^{10} M_\odot$, which is fixed throughout the paper. The radial functions r_1 and r_2 are defined as

$$r_1 = \left\{ \left[\left(\frac{x}{x_0} \right)^2 + \left(\frac{y}{y_0} \right)^2 \right]^2 + \left(\frac{z}{z_0} \right)^4 \right\}^{1/4} \quad (2)$$

and

$$r_2 = \left[\frac{q^2(x^2+y^2)+z^2}{z_0^2} \right]^{1/2}, \quad (3)$$

where the principal axes of the bar are $x_0 = 1.49$ kpc, $y_0 = 0.58$ kpc, $z_0 = 0.40$ kpc and the bulge axis ratio is $q = 0.6$.

2.2 Disc potential and density

We do not include explicitly any dark halo in our potential. Klypin et al. (2002) shows that the dark halo has to be very low in mass in the central part in order to allow many microlensing events by baryonic material. Instead of the usual halo plus exponential disk, we use a Miyamoto-Nagai potential to represent the disk plus halo. The disk potential is given by

$$\Phi_d(x,y,z) = -\frac{GM_d}{r_3}, \quad (4)$$

where

$$r_3 = \left\{ x^2 + y^2 + \left[a_{\rm MN} + (z^2 + b_{\rm MN}^2)^{1/2} \right]^2 \right\}^{1/2}, \quad (5)$$

$a_{\rm MN} = 6.5$ kpc, $b_{\rm MN} = 0.26$ kpc and $M_{\rm d}$ is the total disc mass. In ZH06, $M_{\rm d} = 8 M_{\rm bar}$ and $M_{\rm bar} = 2 \times 10^{10} M_\odot$ is the total mass of the bar. In this paper, we will consider different values of the disk mass but keep the bar mass fixed.

The density distribution of the MN disk is given by

$$\rho_{\rm d}(x,y,z) = \left(\frac{b_{\rm MN}^2 M_d}{4\pi} \right) \times \frac{a_{\rm MN} R^2 + (a_{\rm MN} + 3\sqrt{z^2 + b_{\rm MN}^2})(a_{\rm MN} + \sqrt{z^2 + b_{\rm MN}^2})^2}{[R^2 + (a_{\rm MN} + \sqrt{z^2 + b_{\rm MN}^2})^2]^{5/2} (z^2 + b_{\rm MN}^2)^{3/2}}$$

where $R^2 = x^2 + y^2$.

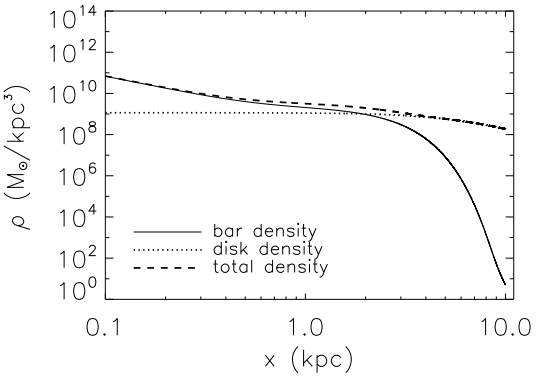

Figure 2. Density distribution along the major (x-) axis. The solid, dotted and dashed lines represent the bar, disk and total density of the model, respectively.

2.3 Density, potential and accelerations of the system

Figure 2 shows the density distribution for the models along the major axis (x-axis). It is obvious that the bar dominates the mass distribution of the system in the inner 3 kpc.

In order to solve the Poisson's equation, we follow Hernquist & Ostriker (1992) and Zhao (1996) to expand the potential and density on a set of simple orthogonal basis of potential-density pairs in the spherical coordinates

$$\Phi_{\rm bar} = -\frac{GM_{\rm bar}}{r_{\rm s}} \sum_{n,l,m} A_{nlm}\Phi_{nlm}, \tag{6}$$

where

$$\Phi_{nlm} = \frac{s^l}{(1+s)^{2l+1}} G_n^{(2l+3/2)}\left(\frac{s-1}{s+1}\right) P_{lm}(\cos\theta)\cos(m\phi), \tag{7}$$

$$s = \frac{r}{r_{\rm s}}, r_{\rm s} = 1 \text{ kpc} \tag{8}$$

and $G_n^{(2l+3/2)}(\xi)$ is the Gegenbauer polynomial of ξ. The expansion coefficient A_{nlm} can be calculated by

$$\begin{aligned} A_{nlm} &= \frac{1}{I_{nl}} \int_{-1}^{1} \frac{2}{(1-\xi)^2} d\xi \int_{-1}^{1} dX \int_{0}^{2\pi} d\phi \rho(r,\theta,\phi) \\ &\times \left[RR(r) P_{lm}(X)\cos(m\phi) \right], \end{aligned} \tag{9}$$

where $\xi = \frac{r-1}{r+1}$, $X = \cos\theta$,

$$RR(r) = \frac{s^l}{(1+s)^{2l+1}} G_n^{(2l+3/2)}(\xi) r^2, \tag{10}$$

$$\begin{aligned} I_{nl} &= K_{nl} \frac{1}{2^{8l+6}} \frac{\Gamma(n+4l+3)}{n!(n+2l+3/2)[\Gamma(2l+3/2)]^2} (1+\delta_{m0})\pi \\ &\times \frac{2}{2l+1} \frac{(l+m)!}{(l-m)!}, \end{aligned} \tag{11}$$

$$K_{nl} = \frac{1}{2} n(n+4l+3) + (l+1)(2l+1) \tag{12}$$

and δ_{m0} is the Dirac Delta function which is defined as $\delta_{m0} = 1$ for $m = 0$ and $\delta_{m0} = 0$ for $m \neq 0$.

Table 1. Twenty Hernquist-Ostriker expansion coefficients A_{nlm}.

n	l	m	A_{nlm}
0	0	0	1.509
1	0	0	-0.086
2	0	0	-0.033
3	0	0	-0.020
0	2	0	-2.606
1	2	0	-0.221
2	2	0	-0.001
0	2	2	0.665
1	2	2	0.129
2	2	2	0.006
0	4	0	6.406
1	4	0	1.295
0	4	2	-0.660
1	4	2	-0.140
0	4	4	0.044
1	4	4	-0.012
0	6	0	-5.859
0	6	2	0.984
0	6	4	-0.030
0	6	6	0.001

Each expansion coefficient is determined by the three quantum numbers n, l, and m. For a triaxial model, only the even quantum number terms are non-zero. The circular velocity profile is shown in Figure 3 along the intermediate axis (y-axis). As can be seen, there is little difference between models with 20 and 40 terms (left panel). So in this paper we will adopt twenty expansion coefficients in the orbit integration to save CPU time. They are listed in Table 1. The right panel of Figure 3 shows the dependence of the circular velocity on the disk mass. Clearly, the model with the massive disk mass has the large circular velocity beyond 1 kpc. Figure 4 shows the contour of effective potentials of the model in the $x-y$ plane (top panel) and $x-z$ planes (bottom panel).

Since we have the potential for the systems, the accelerations can be easily calculated from the potential; we do not give detailed expressions for the acceleration here.

3 MODEL CONSTRUCTION

3.1 Orbit-superposition technology

Since Schwarzschild (1979) pioneered the orbit-superposition method to construct self-consistent models for three-dimensional mass distribution, it has been widely applied in dynamical modelling (e.g. Rix et al. 1997; van der Marel et al. 1998; Binney 2005; van de Ven et al. 2006; Capuzzo-Dolcetta et al. 2007; van den Bosch et al. 2008; Wang et al. 2008; Wu et al. 2009). The key point of this method is to construct an orbit library which is sufficiently comprehensive in order to reproduce the available observations.

Specifically, let $N_{\rm o}$ be the total number of orbits and $N_{\rm c}$ be the number of spatial cells. For each orbit j, we count the fraction time O_{ij} and projected quantities P_{ij} that they spend in each cell i. The fraction time of O_{ij} of each orbit is

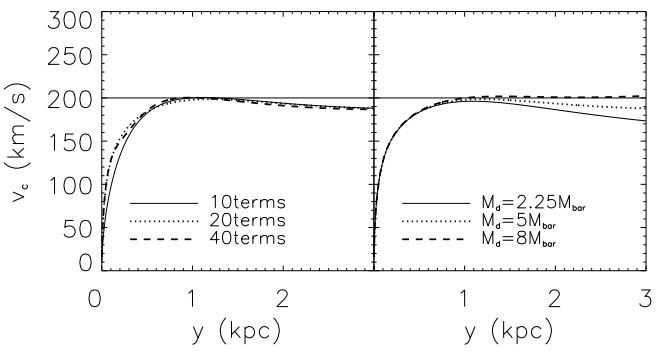

Figure 3. Circular velocity along the intermediate (y-) axis of the bar. *Left*: The solid, dotted and dashed lines represent the results from 10, 20 and 40 terms of the Hernquist-Ostriker expansions, respectively. The disk mass is $\mathrm{M_d} = 1.0 \times 10^{11}\mathrm{M_\odot}$. The flat horizontal line indicates an amplitude of $200\,\mathrm{km\,s^{-1}}$. *Right*: The solid, dotted and dashed lines represent results of $M_\mathrm{d} = 2.25$, 5 and $8M_\mathrm{bar}$, respectively. Twenty terms of Hernquist-Ostriker expansions are used.

obtained as follows. Every orbit is integrated for one Hubble time (t_H), and $N = 10,000$ output (position and velocity) are stored at constant time interval for each each orbit. If the orbit j crosses the cell i one time, we will increase the number N_{ij} by 1. Then, the fraction O_{ij} is determined by $O_{ij} = N_{ij}/N$. The orbit weight W_j for each orbit j is then determined by the following equations:

$$\mu_i = \frac{\sum_{j=1}^{\mathrm{N_o}} W_j O_{ij} P_{ij}}{\sum_{j=1}^{\mathrm{N_o}} W_j O_{ij}}, \qquad i = 1, ..., N_\mathrm{c} \tag{13}$$

where μ_i can be the volume density, surface density, or moments of the velocity distribution in each cell i. If μ_i is the mass or the velocity, then equation (13) is same as equation (2.4) or (2.5) of Pfenniger (1984). Following ZH96, we divide the first octant into 1000 cells with similar masses. Due to symmetry of the model, the other octants are "reflected" to the first octant. In each (x-, y-, and z-) direction, the system is divided into 10 bins. Each cell is a small box with $dx = 0.25\,\mathrm{kpc}$, $dy = 0.15\,\mathrm{kpc}$ and $dz = 0.10\,\mathrm{kpc}$. The central cell covers the box with $x = [-0.25, 0.25]$, $y = [-0.15, 0.15]$ and $z = [-0.1, 0.1]$.

More practically, equation 13 can be written as a set of linear equations

$$\sum_{i=1}^{\mathrm{N_c}} (\mu_i - P_{ij}) O_{ij} W_j = 0 \tag{14}$$

We adopt the non-negative least squares (NNLS) method (Pfenniger 1984) to solve W_j, i.e., the following χ^2_w

$$\chi^2_w = \left| \sum_{i=1}^{\mathrm{N_c}} (\mu_i - P_{ij}) O_{ij} W_j \right|^2 \tag{15}$$

is minimized with respect to W_j ($j = 1, ..., N_\mathrm{o}$) to obtain the values of $W_j \geqslant 0$. It is obvious that the NNLS fit will find a unique solution if the number of orbits is smaller than the number of constraints. However, such a model may not be self-consistent. A more meaningful result with the NNLS

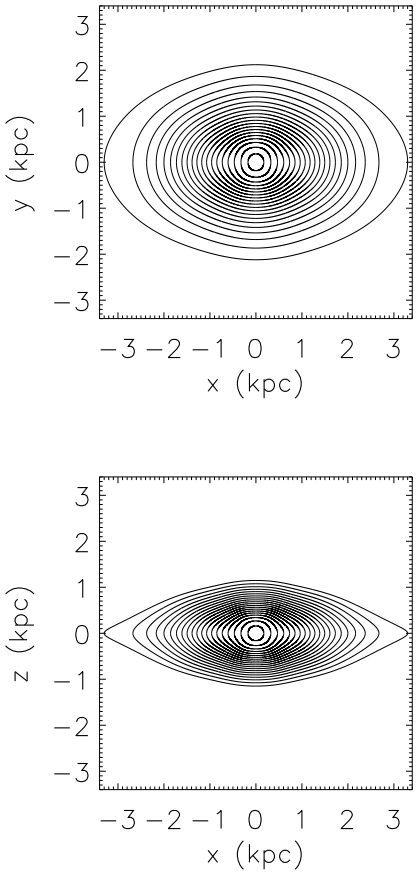

Figure 4. Top: Effective-potential contours for 20 shells with equal mass in the $x-y$ plane. Bottom: Effective-potential contours in the $x-z$ plane. The value of effective potentials in the most inner and outer surfaces are -1.81×10^5 and $-1.08\times10^5(\mathrm{km\,s^{-1}})^2$, respectively.

method should use a large number of smooth orbits well sampled in the phase space. In this case, many exact solutions with $\chi^2 = 0$ are possible. The NNLS method will select one of the possible solutions.

Our density model is smooth, therefore, we expect that the phase-space density from the reconstructed self-consistent model is also smooth. We employ a simple smoothing procedure to fit the data. We require simply that the orbits with adjacent initial conditions have nearly the same weight (Merritt & Fridman 1996, hereafter MF96). In this approach, Equation 15 becomes,

$$\chi^2_w = \left| \sum_{i=1}^{\mathrm{N_c}} (\mu_i - P_{ij}) O_{ij} W_j \right|^2 + \lambda \sum_{j=1}^{\mathrm{N_o}} W_j^2 \tag{16}$$

where λ is a smoothing parameter and $\lambda = N_\mathrm{o}^{-2}$.

MF96's method strongly depends on the size of the cells. In order to assess whether the smoothing method affects our results, we also used another smoothing method, also adopted by ZH96. The key point of this smoothing method is that orbits with similar integrals of motion should have similar orbit weights. In a rotational bar system, only Jacobi's

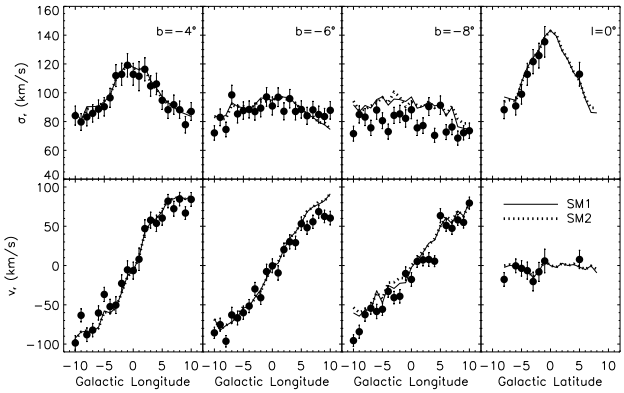

Figure 5. Radial velocity and velocity dispersion along four strips with $b = -4°$, $b = -6°$, $b = -8°$ and $l = 0°$. The solid (SM1) and dotted (SM2) lines indicate the results from our models using the smoothing method as shown in M96 and ZH96, respectively. The filled circles with error bars are data from BRAVA (Kunder et al. 2012).

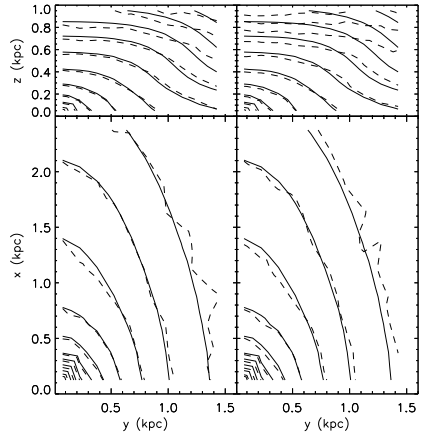

Figure 6. Density contours for the input model (solid lines) and from orbits (dashed lines) in the $x-y$ and $y-z$ planes. The left and right panels represent the results from IC1 and IC2, respectively (see §3.2).

integral E_J is an integral of motion (Binney & Tremaine 1987), here we take the time averaged quantities $\langle L_z \rangle$ and $\langle L_x^2 \rangle$ as the effective integrals, where L_z and L_x are an orbit's instantaneous angular momentum components along the minor and major axes, respectively. Orbits with similar E_J, $\langle L_z \rangle$ and $\langle L_x^2 \rangle$ have similar orbit weights. We have checked the results from these two smoothing methods and found no significant difference (See Figure 5) in their abilities to fit the BRAVA data. The only difference is that we find the MF96's method yields more orbits with non-zero weights than those of ZH96. From now on, we only present results using the smoothing method in M96.

3.2 Constructing the orbit library

In a rotational triaxial system, as mentioned before only Jacobi's energy is an integral of motion. Early studies have shown that most orbits are chaotic (Voglis et al. 2007; Manos & Athanassoula 2011, see also section 4.3.2) and the typical regular orbits are x_1-type (Binney & Tremaine 1987; Zhao 1994; Zhao et al. 1994) in a bar model. We do not know the explicit phase space distribution $f(x, y, z, v_x, v_y, v_z)$ for the chaotic orbits because they lack integrals of motion in a rotating bar potential, we will thus consider two different methods to generate the initial conditions of orbits. The common point of these methods is that the bar model is divided into 20 shells with nearly equal mass spatially along the x-axis by using the Monte Carlo integration (see Fig. 4).

The first method (IC1) is similar to the one adopted in ZH96. Here we give a brief description of its main ingredients, and refer the reader to Appendix B in ZH96 for more details. The orbits are launched in close pairs perpendicular to the $xz-$, $yz-$ or $xy-$ symmetry plane or the x, y axis. The initial position of each orbit in each shell has the same effective potential, which is defined as that in the bounded surface of two close shells. The initial velocity is tangential and less than the local circular velocity. Only 1000 initial conditions of orbits were generated in ZH96, here we extend the number of orbits to $\sim 20,000$.

The second method (IC2) is similar to the one used in Häfner et al. (2000). The initial conditions are generated with known distribution functions $f = \sum_{i=1}^{3} C_i \rho(x, y, z) h_i$, where $C_i, i = 1, 2, 3$ are three normalizing constants, ρ is the density distribution of the system. The three functions $h_{i=1,2,3}$ are defined as

$$h_3(v_x, v_y, v_z) = \frac{1}{(2\pi)^{3/2}\sigma_x\sigma_y\sigma_z} \exp\left(-\frac{v_x^2}{2\sigma_x^2} - \frac{v_y^2}{2\sigma_y^2} - \frac{v_z^2}{2\sigma_z^2}\right) \quad (17)$$

and

$$h_{1,2}(v_R, v_\phi, v_z) = \frac{1}{(2\pi)^{3/2}\sigma_R\sigma_\phi\sigma_z} \times \exp\left[-\frac{v_R^2}{2\sigma_R^2} - \frac{(v_\phi \mp v_{c1})^2}{2\sigma_\phi^2} - \frac{v_z^2}{2\sigma_z^2}\right] \quad (18)$$

where v_{c1} is defined by

$$v_{c1}(R) = 250\,\mathrm{km\,s^{-1}}\left[1 + \left(\frac{0.1\ \mathrm{kpc}}{R}\right)^{0.2}\right]^{-1}. \quad (19)$$

For the velocity dispersion parameters, we adopt the same values as listed in Table 2 of Häfner et al. (2000). We select 50,000 initial conditions using this method.

In Figures 6 and 7, we present the volume density and the projected density contours for model 25 (see Table 1), respectively. In each figure, the solid and dashed lines represent the results from the input and orbit models, respectively. The left and right panels represent the results from the two methods (IC1 and IC2), respectively. It is seen that the orbit from both methods can reproduce the density distribution and projected density distribution well. The difference between the reconstructed and input densities is small, which indicates that our model is self-consistent.

Figure 8 further compares the velocity and velocity dispersion from the model with those from the BRAVA data. There is no significant difference between the results from these two initial conditions, thus from now on, we only present results from the first method (IC1).

As pointed out by Pfenniger (1984), a reasonable orbit integration time may be determined by the fluctuation of the O_{ij} between two successive halves of the integration time.

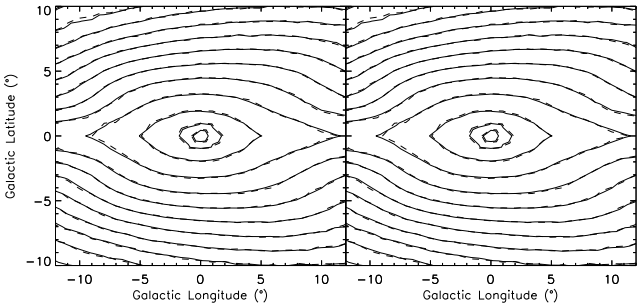

Figure 7. Similar to Figure 6, but for the projected surface density.

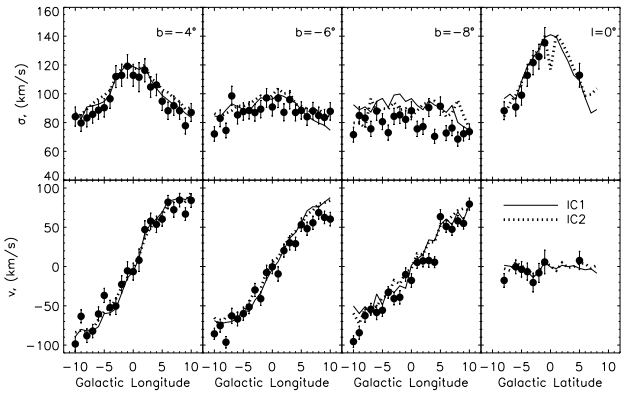

Figure 8. *BRAVA* data versus model as in Figure 5. The solid (IC1) and dashed (IC2) lines indicate the results from our model, while the filled circles with error bars are data from BRAVA.

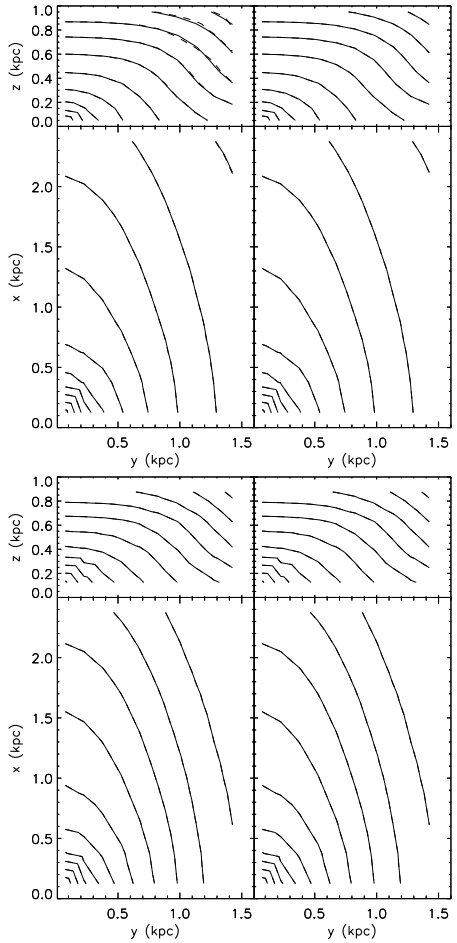

Figure 9. Mass distribution for the input model (solid lines) and from orbits (dashed lines) in the $x-y$ and $y-z$ planes. The left and right panels represent the results from the first and second half Hubble time. Top: Results for using 1000 cells. Bottom: Results for using 400 cells.

The O_{ij} actually reflects the orbit densities and a superposition of O_{ij} reflects the system density. For regular orbits, O_{ij}'s can reach stable values in a relatively short time. However, O_{ij}'s for irregular orbits only can converge after a very long integration time, at least 1000 Hubble times as suggested by Pfenniger (1984). In practice, it will be too time-consuming to integrate a large number of orbits for such a long time. We have compared the fluctuation of the O_{ij}'s between two successive halves in one Hubble time with those in ten Hubble times for irregular orbits, there is no clear improvement in the convergence. In this paper, the orbits are integrated for one Hubble time unless stated otherwise. Although the typical fluctuation of O_{ij}'s is about $\sim 20\%$ between the first and second half, the typical mass fluctuation in each cell is small (below 2%), as can be seen from Figure 9. Figure 9 shows the mass distribution when the integration time is the first and second half Hubble time respectively. We only consider the mass distribution in Equation (15), and no smoothing is adopted. In order to decrease the fluctuation, we decrease the spatial resolution of cells, reducing the cell number from 1000 to 400 by merging every two and half adjacent cells into one along the z-direction. The typical fluctuation of the O_{ij} between the first and second half Hubble time is reduced to $\sim 10\%$ and the mass fluctuation is $\sim 0.05\%$.

Since there are many parameters in the bar model, unless stated otherwise, we adopt $M_{\rm bar} = 2.0 \times 10^{10} M_{\odot}$, $M_{\rm d} = 8M_{\rm bar}$, $\Omega_{\rm p} = 60$ km s^{-1} kpc^{-1} and bar angle $\theta_{\rm bar} = 13.4°$. These parameters are the same as those used in ZH96 (model 25 in Table 2) for ease of comparisons with ZH96.

4 RESULTS

4.1 Model constraints

The key point is to solve the orbit weights from equation 15. To do this, the volume density, projected density, radial velocity and velocity dispersion along four windows $b = -4°$, $b = -6°$, $b = -8°$ and $l = 0°$ (see Figure 5) are used as constraints to solve the weight of each orbit. The volume density and projected density are obtained directly from the density distribution of the bar and Miyamoto-Nagai disk model. Since our aim is to construct a self-consistent bar model, the volume density is fitted only inner 3kpc around the Galactic center.

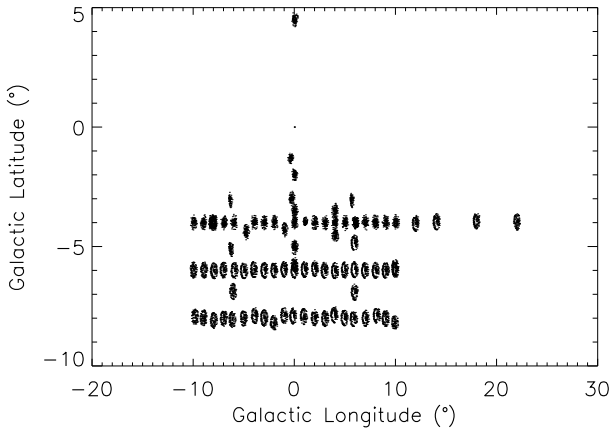

Figure 10. Observed fields by the BRAVA survey from 2005 to 2008 (also see Fig. 1 in Kunder et al. (2012)).

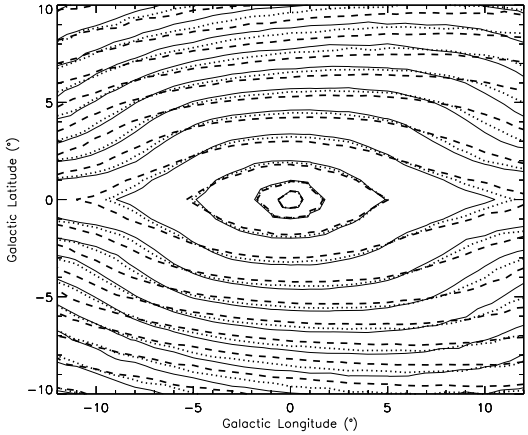

Figure 11. Projected density of the input bar model for different bar angles. The solid, dotted, and dashed lines represent the results for the bar angle 13.4°, 20°, and 30°, respectively.

The kinematic constraints (radial velocity and dispersion) are from the BRAVA survey, conducted from 2005 to 2008 in 8746 fields, which are shown in Figure 10. It is seen that most data are located in the range $l = [-12°, 12°]$ and $b = [-10°, 10°]$, where l is the Galactic longitude and b is the Galactic latitude. In this paper, we fit the projected density, the radial velocity and velocity dispersion in the range $l = [-12°, 12°]$, $b = [-10°, 10°]$.

4.2 Dependence on model parameters

In this subsection, we vary the model parameters around the ZH96 model (model 25 in Table 2) to see the trends. We will explore the parameter space more systematically in section 4.3.

4.2.1 Bar angle

From the COBE map, we know that there is a clear offset between the major axis of the bar and the line-of-sight to the Galactic center. However, its value is not accurately known. From COBE observations, Dwek et al. (1995) found the value of bar angle is $20° \pm 10°$. Using the same COBE map, Zhao (1994) obtained a bar angle 13.4° while Binney et al. (1997) found 20°. Alcock et al. (2000) found this value to be 15°. Recently, the 6.7-GHz methanol masers showed a 45° orientation of bar angle (Green et al. 2011). No consensus appears to be emerging among the recent observations concerning the bar angle.

In Figure 11, we show the projected density maps of the input bar model for different bar angle. It is clear that the isodensity maps become more sharp-edged with an increasing bar angle, which means that the bar angle can be determined if high quality surface brightness data are available. In this paper, our bar model is from ZH96, which attempts to match COBE observations. We can vary the bar angle from 13.4° to 20° or even 30° within the error bar of the model. However, a large bar angle (40°) would require us to refit data in terms of other bar parameters (lengths and axial ratios, Zhao et al. 1996). Therefore, we restrict ourselves to three different bar angles 13.4°, 20° and 30°.

Figure 12 compares the radial velocity and velocity dispersion from the orbit projection with ones from the BRAVA data for different angles. There is a small difference between the results from different bar angles. However, it is clear that kinematics alone constrain the bar angle poorly.

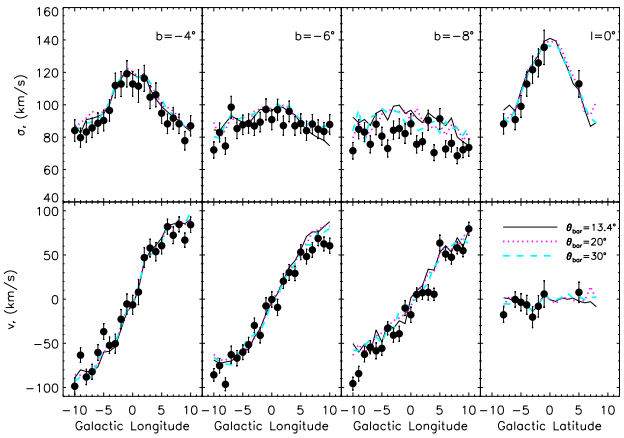

Figure 12. Radial velocity and velocity dispersion along the bulge major axis for different bar angles. The pattern speed is $\Omega_{\rm p} = 60\ {\rm km\,s^{-1}\,kpc^{-1}}$ and $M_{\rm d} = 8M_{\rm bar}$, where $M_{\rm bar} = 2 \times 10^{10} M_{\odot}$.

4.2.2 Pattern speed

The pattern speed of the Galactic bar has been estimated from different methods and are somewhat uncertain. Debattista et al. (2002) used the Tremaine-Weinberg continuity method to the OH/IR stars and obtained a value $\Omega_{\rm p} = (59 \pm 5 \pm 10)\,{\rm kms^{-1}\ kpc^{-1}}$. Englmaier & Gerhard (1999) obtained $\Omega_{\rm p} \approx 60\,{\rm kms^{-1}kpc^{-1}}$ by comparing the gas flow in hydrodynamic simulations with the velocity curve from HI and CO observations. From the length of the bar (Binney et al. 1997; Benjamin et al. 2005; Cabrera-Lavers et al. 2007), the pattern speed was given in a wide range $\Omega_{\rm p} \sim (35 - 60)\ {\rm kms^{-1}kpc^{-1}}$ (Gerhard 2010).

We consider four pattern speeds $\Omega_{\rm p} = 40$, 50, 60 and 80 ${\rm kms^{-1}kpc^{-1}}$. In Figure 13, we present the velocity and velocity dispersion distributions for different pattern speeds. Obviously, the velocity dispersion profile strongly depends

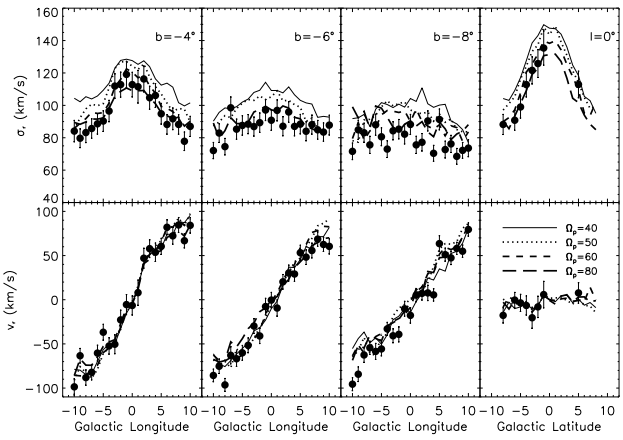

Figure 13. Similar to Figure 12, but for different pattern speeds of the bar. The solid, dotted dashed and long dashed lines represent $\Omega_{\rm p}$ = 40, 50, 60 and 80 km s^{-1} kpc^{-1}, respectively. $M_{\rm d} = 8M_{\rm bar}$, $\theta_{\rm bar} = 20°$.

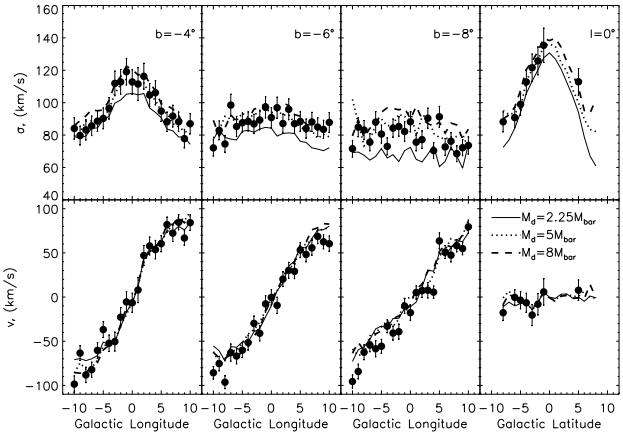

Figure 14. Similar to Figure 12, but for different values of the disk mass. The solid, dotted and dashed curves represent $M_{\rm d}$ = 2.25, 5 and 8 $M_{\rm bar}$, respectively. $\Omega_{\rm p} = 60$ km s^{-1} kpc^{-1}, $\theta_{\rm bar} = 20°$.

on the pattern speed. The predicted velocity dispersion of a model is inversely correlated with its pattern speed.

4.2.3 Disc mass

The disk mass is another parameter which is not accurately known. We consider three different values of the disk mass. Figure 14 shows the dependence of the velocity and velocity dispersion on the disk mass. As can been seen, the velocity dispersion profile from the model strongly depends on the value of the disk mass: as expected, a less massive disk induces a lower velocity dispersion than a more massive one.

4.3 Best-fit model

As mentioned in section 4.2, the kinematics from the model depend on the bar angle, pattern speed and disk mass. In principle, we can divide the parameter space of the bar angle, patter speed and disk mass into many cells. In each parameter cell, we can run the orbit-superposition technique and use the χ^2 fit to find the best-fit parameters. However, numerical calculation is expensive. Here, we calculate 36 models with different parameters (bar angle, pattern speed and disk mass). The χ^2 is defined as

$$\chi^2 = \sum_{i=1}^{\rm N_d} \frac{(y_{\rm obs} - y_{\rm model})^2}{\sigma^2_{\rm obs}}, \tag{20}$$

where $\rm N_{obs}$ is the total number of observed data, $y_{\rm obs}$ and $y_{\rm model}$ are the observed and model kinematics, respectively. Since the three-dimensional and projected densities are given by the input model, we do not include them in the χ^2 fitting, although we do compare the predicted distributions with data by eyes.

Table 2 lists the value of χ^2 for fitting velocity and velocity dispersion along both the major and minor axis of the bar for 36 models. It is seen that models 12, 13, 14, 15, 22, 23, 24, 33 have smaller values of χ^2 than others. visual examination indicates that model 23 is the best-fit model in both the three-dimensional and projected density distributions. Therefore, we choose it as the best-fit model for the BRAVA data.

In Figures 15 and 16, we present the volume density and the projected density contours, respectively. In each figure, the solid and dashed lines represent the results from the input and orbit models, respectively. It is seen that the orbit from model 23 can reproduce the density distribution and projected density distribution well. Moreover, we also use a parameter δ to describe the departure from self-consistency for model 23, which is defined as (MF96):

$$\delta = \sqrt{\chi^2_w}/\bar{M}, \tag{21}$$

where $\bar{M}$ is the average mass in each cell, if the total mass is 1, then $\bar{M} = 1/N_c$. The χ^2_w is obtained from equation 15 by only using the mass constraints and without smoothing. Figure 17 shows the departure from self-consistency as a function of the number of orbits. It is noted that departure parameter δ strongly depends on the number of orbits and the cell number, δ is smaller than 10^{-6} (0.013) when 17,323 orbits are adopted in equation 15 by using the 400 (1000) mass cells, which again shows that model 23 is nearly self-consistent.

The velocity and velocity dispersion distributions of model 23 in Figure 18. Note that model 23 can fit the BRAVA data well with only a few outliers.

4.3.1 Predicted proper motions

Proper motions are not taken into consideration in solving Equations 15 and 16 because the absolute values of proper motions can not be obtained from observations at present due to the lack of absolute astrometry. We can still compare the predicted proper motion dispersions with those observed. Table 3 shows the proper motions in some observed fields together with the predictions from model 23. It is seen that the proper motions along the latitude from model 23 in the Baade's and Sagittarius's Window are in good agreement with those in observations, while the latitudinal proper motion in the Plaut's Window is lower than that in observations. The predicted proper motions along the longitude in the three windows are greater than observed. There are also more proper motion data in small

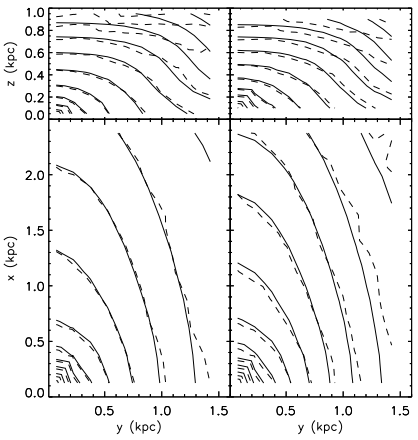

Figure 15. Density contours from the input model (solid lines) and from orbits (dashed lines) in the $x-y$ and $y-z$ planes for model 23. The left and right panes show the results by using 1000 and 400 mass cells, respectively.

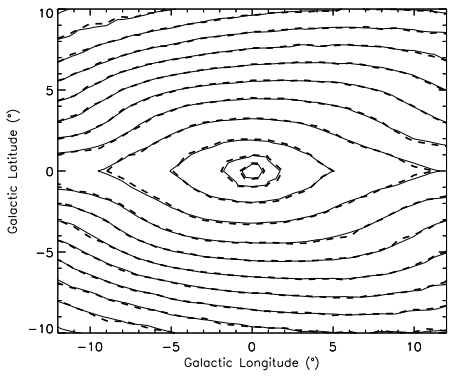

Figure 16. Projected density contours from the input model (solid lines) and from orbits (dashed lines) for model 23. 1000 cells are used for solving the orbit weight.

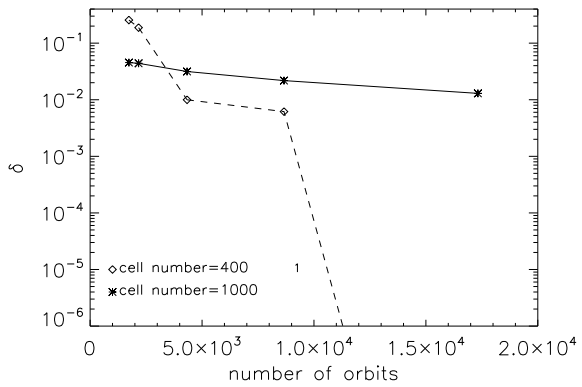

Figure 17. Departure from self-consistency δ as a function of the number of orbits. The star and diamond symbols represent the fitting results by using 1000 and 400 mass cells, respectively.

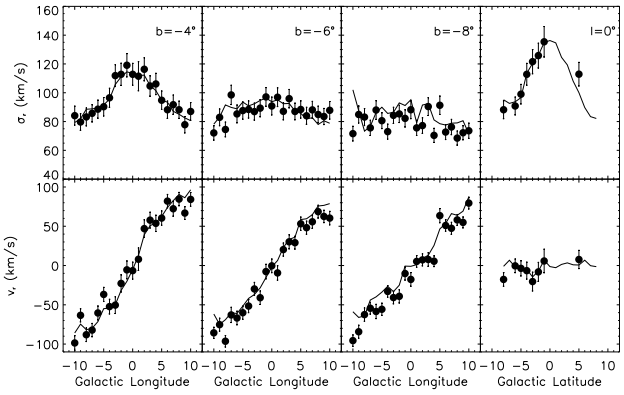

Figure 18. Velocity and velocity dispersion distribution for model 23 ($\Omega_{\rm p} = 60$ km s^{-1} kpc^{-1}, disk mass $\rm M_d = 1.0\times10^{11}M_\odot$ and bar angle $\theta_{\rm bar} = 20°$). The solid line is for the model while the filled circles are data from BRAVA.

fields from OGLE (Sumi et al. 2004; Rattenbury et al. 2007; Rattenbury & Mao 2008) and HST (Kozłowski et al. 2006), we do not compare with the proper motion in these field because the sky area in our model is $1° \times 1°$, much larger than the observed field size.

4.3.2 Phase-space distribution and orbit families

The phase-space distribution and the orbit family are useful to help us understand the model. Figure 19 shows the distribution of average energy versus angular momentum along the z-axis for non-zero weight orbits. The solid and dashed lines are the theoretical distributions of the energy versus angular momentum along the z-axis for retrograde and prograde motions from 0 to 3kpc, respectively. The energy and angular momentum along the z-axis in the laboratory frame are defined as $E_{\rm lab}(r) = \Phi(r) + [\pm|V_{\rm c}|]^2/2$, $J_{\rm z,lab}(r) = [\pm|V_{\rm c}|] \times r$. In the rotating frame, they are $E_{\rm rot}(r) = \Phi(r) + [\pm|V_{\rm c}| + |\Omega_{\rm p}|r]^2/2$, and $J_{\rm z,rot}(r) = [\pm|V_{\rm c}| + |\Omega_{\rm p}|r] \times r$. Here r is the radius, $V_{\rm c}$ is the circular velocity and Φ is the potential of the system. The '+' and '-' signs mean the retrograde/prograde motions. It is seen that most orbits are located in the range between the prograde and retrograde motions; only small number of orbits are disk orbits. For the orbit classification, we use the method of Carpintero & Aguilar (1998). In Table 5, we show the relative fractions of orbit families with non-zero weights for model 23. It is seen that irregular orbits dominate the orbit families, the fraction of these orbits is over 90% for the models if the integration time is one Hubble time. We also find that the relative orbit fraction strongly depends on the integrated orbit time, the fraction of irregular orbits increases with increasing orbit integration time.

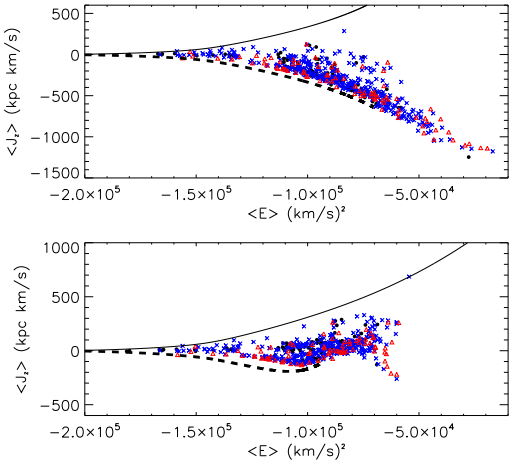

Figure 19. Distribution of the average energy versus angular momentum along the z-axis for orbits with non-zero weights. The upper and lower panels show the results in the laboratory and rotational frames, respectively. The filled circles, crosses and triangles represent orbits with large, intermediate and small weights, respectively. The solid and dashed lines represent the theoretical retrograde and prograde motions from 0 to 3kpc, respectively. The bar model is model 23 with $\Omega_{\rm p} = 60$ km s^{-1} kpc^{-1}, $M_{\rm d} = 5.0 \times M_{\rm bar}$ and $\theta_{\rm bar} = 20°$.

Table 2. χ^2 for different input models, which are constrained by the velocity and velocity dispersion in four windows ($b = -4°, b = -6°, b = -8°$ and $l = 0°$).

model ID	$\Omega_{\rm p}$ (km s^{-1} kpc^{-1})	$M_{\rm d}$ ($M_{\rm bar}$)	$\theta_{\rm bar}$ (°)	χ^2
1	40	2.25	13.4	331
2	40	2.25	20	328
3	40	2.25	30	430
4	40	5	13.4	359
5	40	5	20	393
6	40	5	30	438
7	40	8	13.4	851
8	40	8	20	902
9	40	8	30	843
10	50	2.25	13.4	363
11	50	2.25	20	340
12	50	2.25	30	272
13	50	5	13.4	297
14	50	5	20	279
15	50	5	30	284
16	50	8	13.4	606
17	50	8	20	633
18	50	8	30	561
19	60	2.25	13.4	456
20	60	2.25	20	444
21	60	2.25	30	379
22	60	5	13.4	308
23	60	5	20	293
24	60	5	30	298
25	60	8	13.4	403
26	60	8	20	354
27	60	8	30	344
28	80	2.25	13.4	314
29	80	2.25	20	374
30	80	2.25	30	371
31	80	5	13.4	319
32	80	5	20	398
33	80	5	30	273
34	80	8	13.4	379
35	80	8	20	352
36	80	8	30	467

Table 3. Observed proper motion dispersions in some fields. The bottom four rows are predictions from model 23.

Field	(l,b)	σ_l	σ_b	Ref.
	(°)	(mas yr^{-1})	(mas yr^{-1})	
Baade's Window	(1,-4)	3.2 ± 0.1	2.8 ± 0.1	Spaenhauer et al. (1992)
Baade's Window	(1,-4)	3.14 ± 0.11	2.74 ± 0.08	Zhao et al. (1996)
Baade's Window	(1.13,-3.77)	2.9	2.5	Kuijken & Rich (2002)
Baade's Window	(1,-4)	2.87 ± 0.08	2.59 ± 0.08	Kozłowski et al. (2006)
Baade's Window	(0.9,-4)	3.06 ± 0.11	2.79 ± 0.13	Soto et al. (2007)
Baade's Window	(1,-4)	3.13 ± 0.16	2.50 ± 0.10	Babusiaux et al. (2010)
Baade's Window	(1.13,-3.76)	3.11 ± 0.08	2.74 ± 0.13	Soto (2012) in preparation
Plaut's Window	(0,-8)	3.39 ± 0.11	2.91 ± 0.09	Vieira et al. (2007, 2009)
Sagittarius I	(1.25,-2.65)	3.3	2.7	Kuijken & Rich (2002)
Sagittarius I	(1.27,-2.66)	3.07 ± 0.08	2.73 ± 0.07	Kozłowski et al. (2006)
Sagittarius I	(1.25,-2.65)	3.067	2.760	Clarkson et al. (2008)
Sagittarius I	(1.26,-2.65)	3.56 ± 0.08	2.87 ± 0.08	Soto (2012) in preparation
NGC 6558	(0.28,-6.17)	2.90 ± 0.11	2.87 ± 0.13	Soto (2012) in preparation
Baade's Window	(1,-4)	4.44	2.52	Model 23
Plaut's Window	(0,-8)	5.28	2.32	Model 23
Sagittarius I	(1,-3)	4.43	2.67	Model 23
NGC 6558	(0,-6)	4.46	2.36	Model 23

Table 4. Tangential velocity dispersion in some fields. The values given in the references are derived from proper motions by assuming a distance to the Galactic centre $R_0 = 8\,\mathrm{kpc}$.

Field	(l,b)	σ_l	σ_b	Ref.
	(°)	(km s^{-1})	(km s^{-1})	
Baade's Window	(1,-4)	121 ± 4	106 ± 4	Spaenhauer et al. (1992)
Baade's Window	(1,-4)	119 ± 4	104 ± 3	Zhao et al. (1996)
Baade's Window	(1.13,-3.77)	111	100	Kuijken & Rich (2002)
Baade's Window	(1,-4)	109 ± 3	98 ± 3	Kozłowski et al. (2006)
Baade's Window	(0.9,-4)	116 ± 4	106 ± 5	Soto et al. (2007)
Baade's Window	(1,-4)	119 ± 6	95 ± 4	Babusiaux et al. (2010)
Baade's Window	(1.13,-3.76)	118 ± 3	104 ± 5	Soto et al. (2012)
Plaut's Window	(0,-8)	129 ± 4	110 ± 4	Vieira et al. (2007, 2009)
Sagittarius I	(1.25,-2.65)	123	108	Kuijken & Rich (2002)
Sagittarius I	(1.27,-2.66)	117 ± 3	104 ± 3	Kozłowski et al. (2006)
Sagittarius I	(1.25,-2.65)	116	105	Clarkson et al. (2008)
Sagittarius I	(1.26,-2.65)	135 ± 3	109 ± 3	Soto et al. (2012)
NGC 6558	(0.28,-6.17)	110 ± 4	109 ± 5	Soto et al. (2012)
Baade's Window	(1,-4)	138	90	Model 23
Plaut's Window	(0,-8)	121	71	Model 23
Sagittarius I	(1,-3)	145	97	Model 23
NGC 6558	(0,-6)	125	78	Model 23
Baade's Window	(1,-4)	140	106	ZH96
Sagittarius I	(1,-3)	146	118	ZH96

Table 5. Relative fractions of orbit families with non-zero weights for model 23.

Orbit families	Fractions[a]	Fraction[b]	Fraction[c]	Fraction[d]
irregular	92.9%	91.2%	81.3%	80.6%
open z tube	5.8%	5.6%	13.5%	12.0%
thin z tube	0.5%	2.2%	2.27%	2.6%
others[e]	0.8%	1.0%	2.93%	4.8%

[a] The integration time of orbits is one Hubble time.
[b] The integration time of orbits is one half Hubble time.
[c] The integration time of orbits is one third Hubble time.
[d] The integration time of orbits is one fourth Hubble time.
[e] others mean closed z tube, open box, open x tube etc.

5 STABILITY OF THE MODEL

A perfect dynamical model must be self-consistent and stable. From the projected density map and radial kinematics, we know that our model is self-consistent. However, its dynamical stability still needs to be demonstrated. For a non-spherical model, N-body simulations can help us check the stability of the model. For this purpose, we use the versatile code GADGET-2 (Springel 2005) to run our galaxy simulation.

One important step in N-body simulations is to generate the initial conditions. In our study, we follow Zhao (1996) and Wu et al. (2009). The total number of initial particles is 2×10^5. They are randomly sampled from non-zero weight orbits. In each orbit, the selected number of particles is proportional to its orbit weight. The disk part is not in equilibrium outside 3 kpc, and 30% of the disk mass escaped during the simulation. The bar is essentially in equilibrium with an overall drift of 2 km s^{-1} perhaps due to the asymmetric escape of the disk particles.

The N-body simulation for our best-fit model 23 is run for 2 Gyr, and 30 snapshots of particle positions and velocities are stored. Figure 20 shows the snapshots of the model at 0, 0.1 and 0.5 Gyr.

Two imperfections are noted: by construction, our disk part is not in equilibrium outside 3 kpc where no self-consistency was imposed in the Schwarzschild model. As a result about 30% of the disk mass evaporates due to the relatively shallow potential of the live particles. The bulk of the disk remains, however, the non-equilibrium of the disk makes it difficult for us to assess the long-term stability of the bar model. Secondly the center of the bar begins to drift slightly from the origin. The drift speed is very low, about 2 km s^{-1}, probably due to the recoil momentum of asymmetric evaporation of disk particles beyond 3 kpc.

Nevertheless an examination of the moment of inertia I_{XY}, I_{XX} and I_{YY} reveals that the bar rotates about 5 times (i.e., there are 10 peaks in I_{XY}, I_{XX} and I_{YY}) in 0.5 Gyrs, which is consistent with a constant pattern rotation speed 60 km s^{-1} kpc^{-1}. The axis ratio appears stable as well with very little evolution within 2 Gyrs. Clearly more runs are necessary with particular attention to include a disk component.

6 CONCLUSION AND DISCUSSION

We have constructed 36 nuclear models using Schwarzschild's method, varying the bar angle, bar pattern speed and disk mass. Through χ^2 fitting, we find the best-fit model has $\Omega_{\rm p} = 60$ km s^{-1} kpc^{-1}, $M_{\rm d} = 1.0 \times 10^{11} M_\odot$ and $\theta_{\rm bar} = 20^\circ$. The model can reproduce the three-dimensional density, surface density and BRAVA velocity and velocity dispersion well. We tested two different methods of smoothing and two methods of generating initial conditions; our results are independent of these.

Compared to the model of ZH96, our model can better reproduce the rotation curve as seen in the average radial velocity and the surface brightness distributions. However, our model is incomplete in at least two aspects, the first is that the predicted proper motions appear to be too high, and the second is the stability of the system is far from perfect. We discuss these two issues in turn.

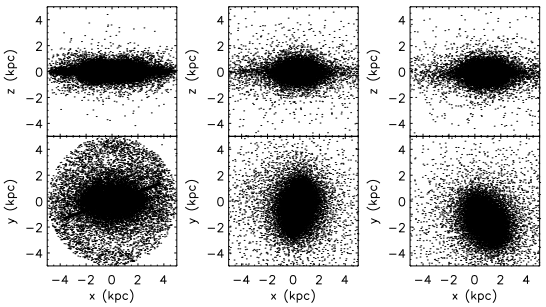

Figure 20. Snapshots for the steady-state model of N-body simulations for model 23. From left to right, the output time is 0, 0.1 and 0.5 Gyr, respectively. The solid line at the bottom left panel indicates the line of sight to the Galactic centre.

The proper motion dispersions in some windows predicted from the model are higher than observed along the Galactic longitude. Possible reasons are:

(i) The nuclear model in our paper is not perfect. Although we have calculated 36 models with different parameters, it is possible that we still miss the model with the right combinations. In particular, we have used a fixed bar mass ($2.0 \times 10^{10} M_\odot$) in this study. Moreover, the density models adopted in this paper are obtained from fitting the surface brightness of the inner Galaxy. It has been shown that models with different axis ratios can fit the surface brightness of the bar (Zhao et al. 1996). In other words, the three-dimensional density distribution is not unique. Our model shows a stronger anisotropic distribution in proper motion than in observations, thus a less triaxial bar model may be preferred.

(ii) The proper motion is obtained by using the orbits inner 5kpc around the Galactic center. If we use the orbits only inner 2.5 kpc around the Galactic center, the predicted value of proper motion will be changed. For example, in BW, $\sigma_l = 3.72$ mas yr^{-1} and $\sigma_b = 2.53$ mas yr^{-1}, then the agreement between the model prediction and observation improves. A useful way to compare the model prediction with those observations is to use both the tangential velocity dispersion and proper motion dispersion. It is seen that the predicted velocity dispersion in the Plaut's Window along the longitude direction is close to the observed value (See Table 4) .

(iii) The predictions in our model are for pixels of $1^\circ \times 1^\circ$, the observed regions are far smaller. The predicted proper motions of model 23 in the range $l = [-12^\circ, 12^\circ]$, $b = [-10^\circ, 10^\circ]$ are available online [1]. Future observations of large proper motion samples can help us to further constrain the models.

The second shortcoming of our model is the dynamical instability. N-body simulations show that the model is only stable for 0.5 Gyr. The initial conditions for N-body

[1] http://cosmology.bao.ac.cn/~ wangyg/

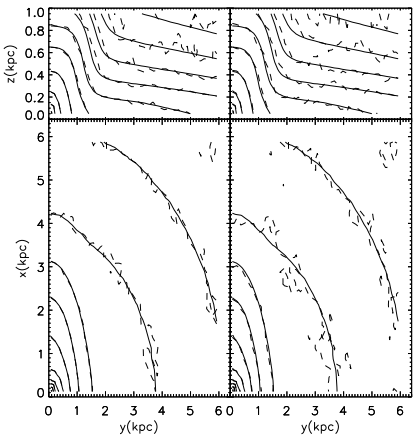

Figure 21. Density contours from the input model (solid lines) and from orbits (dashed lines) in the $x-y$ and $y-z$ planes for model 23. The left panel is for the result of the orbit weights are solved by only using the three-dimensional density while the right one is that the orbit weights are solved by using the three-dimensional density, velocity and velocity dispersion.

are generated from the orbit weights. In our model, most orbits are irregular. The fraction of irregular orbit strongly depends on the potential. Our model includes a prolate bar, a boxy bulge and an axi-symmetric disk; the axis ratios of these three components are different. In particular, the presence of the bar implies the axi-symmetric disk should not be present in the central part since no circular orbits can exist. This may have limited the dynamical stability of our system. In addition, we only consider the self-consistency of the model within 3 kpc. The disk is an important component in our model which dominates the mass beyond 3 kpc. We also check the self-consistency of the model inside 6 kpc, which covers the outer Lindblad resonance region ($\sim$ 6kpc). Figure 21 compares the input and the reconstructed densities from orbits. As can be seen, the agreement is good within 3 kpc, but the scatters become increasingly larger ($\sim$ 30%) beyond 3 kpc. The N-body simulation again shows that the model is only stable within 0.5 Gyr. In the future, it may be desirable to start with a bar model from N-body simulations such as that from Shen et al. (2010).

At present, most density or potential models of the Galactic nucleus are constructed using photometric data (surface brightness and star counts) alone. However, no density model is constructed including the kinematics, such as velocity, velocity dispersion and proper motion. In the future, it may be useful to construct the Galactic bar model using the density and photometry at the same time. Future observations such as GAIA will be particularly valuable to help us construct a density model.

ACKNOWLEDGEMENTS

We thank the referee Daniel Pfenniger for the comments and suggestions. We acknowledge helpful discussions with Juntai Shen, Zuhui Fan, Lia Athanassoula, Simon White, Ortwin Gerhard, Inma Martinez-Valpuesta, and the hospitality of the Aspen Center for Physics. We also thank other members of the BRAVA collaboration, especially A. Kunder, who compiled the final public release dataset, and M. Soto, who provided us the unpublished proper motion data.

This work was started during Y.G.W.'s visit in 2008 to the Jodrell Bank Centre for Astrophysics supported by their visitor's grant. Y.G.W. acknowledges the support by the National Science Foundation of China (Grant No. Y011061001 and No. Y122071001). and S.M. thanks the Chinese Academy of Sciences for financial support. R.M.R. acknowledges support from NSF grant AST0709749, and GO-11655.01.

Most of the computing was performed on the supercomputer "laohu" at the High Performance Computing Center at National Astronomical Observatories of China, funded by Ministry of Finance under the grant ZDYZ2008-2.

REFERENCES

Alcock C., Allsman R. A., Alves D. R., Axelrod T. S., Becker A. C., Bennett D. P., Cook K. H., Drake A. J., Freeman K. C., Geha M., Griest K.and Lehner M. J., Marshall S. L., Minniti D., Nelson C. A.and Peterson B. A., Popowski P., Pratt M. R., 2000, ApJ, 541, 734

Babusiaux C., Gilmore G., 2005, MNRAS, 358, 1309

Babusiaux C., Gómez A., Hill V., Royer F., Zoccali M., Arenou F., Fux R., Lecureur A., Schultheis M., Barbuy B., Minniti D., Ortolani S., 2010, A&A, 519, A77

Benjamin R. A., Churchwell E., Babler B. L., Indebetouw e. a., 2005, ApJ, 630, L149

Binney J., 2005, MNRAS, 363, 937

Binney J., Gerhard O., Spergel D., 1997, MNRAS, 288, 365

Binney J., Tremaine S., 1987, Galactic dynamics

Bissantz N., Debattista V. P., Gerhard O., 2004, ApJ, 601, L155

Blitz L., Spergel D. N., 1991, ApJ, 379, 631

Cabrera-Lavers A., Hammersley P. L., González-Fernández C., López-Corredoira M., Garzón F., Mahoney T. J., 2007, A&A, 465, 825

Capuzzo-Dolcetta R., Leccese L., Merritt D., Vicari A., 2007, ApJ, 666, 165

Carpintero D. D., Aguilar L. A., 1998, MNRAS, 298, 1

Clarkson W., Sahu K., Anderson J., Smith T. E., Brown T. M., Rich R. M., Casertano S., Bond H. E., Livio M., Minniti D., Panagia N., Renzini A., Valenti J., Zoccali M., 2008, ApJ, 684, 1110

de Lorenzi F., Debattista V. P., Gerhard O., Sambhus N., 2007, MNRAS, 376, 71

Debattista V. P., Gerhard O., Sevenster M. N., 2002, MNRAS, 334, 355

Dehnen W., 2009, MNRAS, 395, 1079

Dwek E., Arendt R. G., Hauser M. G., Kelsall T., Lisse C. M., Moseley S. H., Silverberg R. F., Sodroski T. J., Weiland J. L., 1995, ApJ, 445, 716

Englmaier P., Gerhard O., 1999, MNRAS, 304, 512

Gerhard O., 2010, ArXiv e-prints

Gonzalez O. A., Rejkuba M., Minniti D., Zoccali M., Valenti E., Saito R. K., 2011, A&A, 534, L14

Green J. A., Caswell J. L., McClure-Griffiths N. M., Avison A., Breen S. L., Burton M. G., Ellingsen S. P., Fuller G. A., Gray M. D., Pestalozzi M., Thompson M. A., Voronkov M. A., 2011, ArXiv e-prints

Häfner R., Evans N. W., Dehnen W., Binney J., 2000, MNRAS, 314, 433
Hernquist L., Ostriker J. P., 1992, ApJ, 386, 375
Howard C. D., Rich R. M., Reitzel D. B., Koch A., De Propris R., Zhao H., 2008, ApJ, 688, 1060
Klypin A., Zhao H., Somerville R. S., 2002, ApJ, 573, 597
Kozłowski S., Woźniak P. R., Mao S., Smith M. C., Sumi T., Vestrand W. T., Wyrzykowski Ł., 2006, MNRAS, 370, 435
Kuijken K., Rich R. M., 2002, AJ, 124, 2054
Kunder A., Koch A., Rich R. M., de Propris R., Howard C. D., Stubbs S. A., Johnson C. I., Shen J., Wang Y., Robin A. C., Kormendy J., Soto M., Frinchaboy P., Reitzel D. B., Zhao H., Origlia L., 2012, AJ, 143, 57
Lee G.-H., Park C., Lee M. G., Choi Y.-Y., 2011, ArXiv e-prints
Long R. J., Mao S., 2010, MNRAS, 405, 301
Manos T., Athanassoula E., 2011, ArXiv e-prints
Mao S., Paczyński B., 2002, MNRAS, 337, 895
Merritt D., Fridman T., 1996, ApJ, 460, 136
Pfenniger D., 1984, A&A, 141, 171
Rattenbury N. J., Mao S., 2008, MNRAS, 385, 905
Rattenbury N. J., Mao S., Debattista V. P., Sumi T., Gerhard O., de Lorenzi F., 2007, MNRAS, 378, 1165
Rattenbury N. J., Mao S., Sumi T., Smith M. C., 2007, MNRAS, 378, 1064
Rich R. M., Reitzel D. B., Howard C. D., Zhao H., 2007, ApJ, 658, L29
Rix H., de Zeeuw P. T., Cretton N., van der Marel R. P., Carollo C. M., 1997, ApJ, 488, 702
Schwarzschild M., 1979, ApJ, 232, 236
Shen J., Rich R. M., Kormendy J., Howard C. D., De Propris R., Kunder A., 2010, ApJ, 720, L72
Soto M., Kuijken K., Rich R. M., 2012, ArXiv e-prints
Soto M., Rich R. M., Kuijken K., 2007, ApJ, 665, L31
Spaenhauer A., Jones B. F., Whitford A. E., 1992, AJ, 103, 297
Springel V., 2005, MNRAS, 364, 1105
Stanek K. Z., Mateo M., Udalski A., Szymanski M., Kaluzny J., Kubiak M., 1994, ApJ, 429, L73
Stanek K. Z., Udalski A., Szymanski M., Kaluzny J., Kubiak M., Mateo M., Krzeminski W., 1997, ApJ, 477, 163
Sumi T., Wu X., Udalski A., Szymański M., Kubiak M., Pietrzyński G., Soszyński I., Woźniak P., Żebruń K., Szewczyk O., Wyrzykowski Ł., 2004, MNRAS, 348, 1439
Syer D., Tremaine S., 1996, MNRAS, 282, 223
Udalski A., Zebrun K., Szymanski M., Kubiak M., Pietrzynski G., Soszynski I., Wozniak P., 2000, Acta Astron, 50, 1
van de Ven G., van den Bosch R. C. E., Verolme E. K., de Zeeuw P. T., 2006, A&A, 445, 513
van den Bosch R. C. E., van de Ven G., Verolme E. K., Cappellari M., de Zeeuw P. T., 2008, MNRAS, 385, 647
van der Marel R. P., Cretton N., de Zeeuw P. T., Rix H., 1998, ApJ, 493, 613
Vieira K., Casetti-Dinescu D. I., Méndez R. A., Rich R. M., Girard T. M., Korchagin V. I., van Altena W., Majewski S. R., van den Bergh S., 2007, AJ, 134, 1432
Vieira K., Casetti-Dinescu D. I., Méndez R. A., Rich R. M., Girard T. M., Korchagin V. I., van Altena W. F., Majeski S. R., van den Bergh S., 2009, in Revista Mexicana de Astronomia y Astrofisica Conference Series Vol. 35 of Revista Mexicana de Astronomia y Astrofisica Conference Series, Proper Motions in the Galactic Bulge: Plaut's Window. pp 123–124
Voglis N., Harsoula M., Contopoulos G., 2007, MNRAS, 381, 757
Wang Y., Wu X., Zhao H., 2008, ApJ, 677, 1033
Wu X., Zhao H., Wang Y., Llinares C., Knebe A., 2009, MNRAS, 396, 109
Zhao H., 1994, PhD thesis, Columbia Univ.
Zhao H., Rich R. M., Biello J., 1996, ApJ, 470, 506
Zhao H., Rich R. M., Spergel D. N., 1996, MNRAS, 282, 175
Zhao H., Spergel D. N., Rich R. M., 1994, AJ, 108, 2154
Zhao H., Spergel D. N., Rich R. M., 1995, ApJ, 440, L13
Zhao H. S., 1996, MNRAS, 283, 149